Experimental Identification of Bistable Flow States on the Space Launch System at Liftoff Conditions

Morgan A. Walker*, Jeremy T. Pinier†, Patrick R. Shea‡, Jesse G. Collins§, Lee J. Mears¶, Michael W. Lee‖, and Brent W. Pomeroy**
NASA Langley Research Center, Hampton, VA 23681

Time-averaged global force and moment measurements in wind tunnel tests can obscure complex flow dynamics, including bistability phenomena. This paper presents a detailed analysis into the potential cause of previously unobserved discrepancies among repeat runs during the 2021 14- by 22-Foot Subsonic Tunnel test of the Space Launch System. During the test, it was observed that liftoff configuration repeatability was not as strong as expected when compared to previous tests. These discrepancies occurred between wind azimuth angles of approximately 150° and 220°, as well as between 330° and 30°. After ruling out common confounding factors such as instrumentation hysteresis and temperature, it was hypothesized that the lack of repeatability was caused by the Coandă effect producing a bistable flow state at different locations between the cylindrical rocket centerbody and solid rocket boosters during the acquisition of data. Evidence to support this hypothesis is provided in this paper in the form of time-averaged force and moment coefficient data, time-dependent force and moment coefficient data, and still images from smoke flow and tuft flow visualization runs.

Nomenclature

ATI-IA	=	ATI Industrial Automation, Inc.
BLCA	=	left solid rocket booster axial force coefficient at the balance moment center, body axis
BLCLL	=	left solid rocket booster rolling moment coefficient at the balance moment center, body axis
BLCLM	=	left solid rocket booster pitching moment coefficient at the balance moment center, body axis
BLCLN	=	left solid rocket booster yawing moment coefficient at the balance moment center, body axis
BLCN	=	left solid rocket booster normal force coefficient at the balance moment center, body axis
BLCY	=	left solid rocket booster side force coefficient at the balance moment center, body axis
BRCA	=	right solid rocket booster axial force coefficient at the balance moment center, body axis
BRCLL	=	right solid rocket booster rolling moment coefficient at the balance moment center, body axis
BRCLM	=	right solid rocket booster pitching moment coefficient at the balance moment center, body axis
BRCLN	=	right solid rocket booster yawing moment coefficient at the balance moment center, body axis
BRCN	=	right solid rocket booster normal force coefficient at the balance moment center, body axis
BRCY	=	right solid rocket booster side force coefficient at the balance moment center, body axis
CA	=	rocket forebody axial force coefficient at the balance moment center, body axis
CFD	=	Computational Fluid Dynamics
CLL	=	rocket forebody rolling moment coefficient at the balance moment center, body axis
CLM	=	rocket forebody pitching moment coefficient at the balance moment center, body axis
CLN	=	rocket forebody yawing moment coefficient at the balance moment center, body axis
CN	=	rocket forebody normal force coefficient at the balance moment center, body axis
CUI	=	Controlled Unclassified Information
CY	=	rocket forebody side force coefficient at the balance moment center, body axis

*Research Aerospace Engineer, Configuration Aerodynamics Branch, AIAA Member, morgan.a.walker@nasa.gov.
†Research Aerospace Engineer, Configuration Aerodynamics Branch, AIAA Associate Fellow, jeremy.t.pinier@nasa.gov.
‡Research Aerospace Engineer, Configuration Aerodynamics Branch, AIAA Senior Member, patrick.r.shea@nasa.gov.
§Research Aerospace Engineer, Configuration Aerodynamics Branch, AIAA Member, jesse.g.collins@nasa.gov.
¶Research Aerospace Engineer, Configuration Aerodynamics Branch, AIAA Member, lee.j.mears@nasa.gov.
‖Research Aerospace Engineer, Configuration Aerodynamics Branch, AIAA Member, michael.w.lee@nasa.gov.
**Research Aerospace Engineer, Configuration Aerodynamics Branch, AIAA Senior Member, brent.w.pomeroy@nasa.gov.

D	=	sting diameter, in
DAU	=	Data Acquisition Unit
h	=	height of launch vehicle above the mobile launch platform, ft
h/L	=	liftoff ratio
ITAR	=	International Traffic in Arms Regulations
L	=	launch tower height, ft
LOT	=	Liftoff and Transition
LSRB	=	Left Solid Rocket Booster
MIF	=	Model Interface
ML-2	=	Mobile Launcher 2
MLP	=	Mobile Launch Platform
q_∞	=	dynamic pressure, psf
Re_D	=	Reynolds number based on core diameter
RSRB	=	Right Solid Rocket Booster
SDAS	=	Static Data Acquisition System
SLS	=	Space Launch System
SRB	=	Solid Rocket Booster
t	=	time elapsed, sec
X	=	X-coordinate, wind tunnel coordinate system
Y	=	Y-coordinate, wind tunnel coordinate system
Z	=	Z-coordinate, wind tunnel coordinate system
α	=	body axis angle of attack, deg
ψ_{azm}	=	wind azimuth angle, deg

I. Introduction

The Space Launch System (SLS) is a launch vehicle currently under development by NASA that will expand the capabilities of human space exploration beyond Earth's orbit [1]. Each configuration of the SLS vehicle, shown in Fig. 1, is built upon the common design of a liquid fuel core stage coupled with two rocket boosters. The core stage will remain common across all configurations, while the Block 2 designs will be the first to introduce new boosters. Depending on the mission profile, different upper stages can be integrated into this core stage to accommodate the launch of either the crewed Orion module or payload fairings for cargo missions.

In support of the SLS program, the SLS Aerodynamics Task Team is tasked with quantifying the induced environments on the launch vehicle from the liftoff phase until the rocket exits Earth's atmosphere. These aerodynamic environments are quantified through the creation and delivery of aerodynamic databases constructed through a combination of wind tunnel testing programs and CFD simulations.

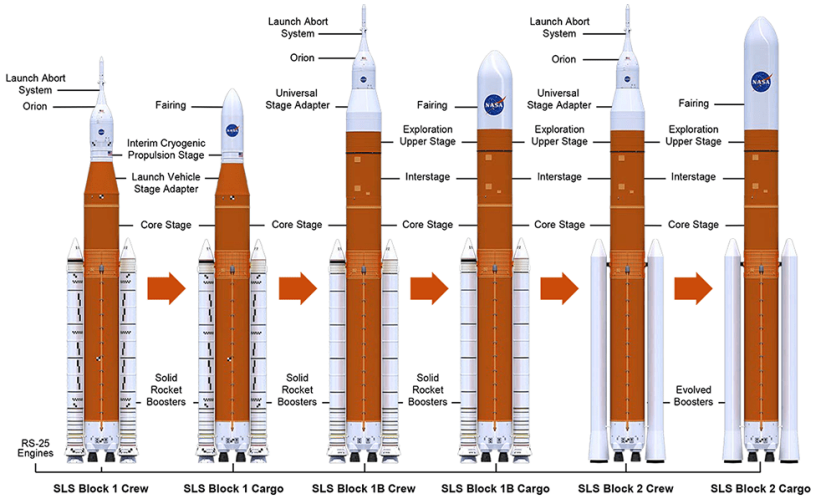

Fig. 1 Artist rendering of the evolving SLS configurations [1].

This paper will focus on a subset of runs that exhibited repeatability concerns during the subsonic wind tunnel test of the 1.75%-scale SLS Block 1B Cargo and Block 1B Crew configuration models. The paper will present an overview of the experimental design used to conduct the subsonic wind tunnel test of the SLS, including a description of the facility, the data acquisition system, the model description, the model instrumentation, and the smoke flow visualization system used. It will then introduce the discrepancies observed in repeat runs of the liftoff configuration and provide evidence supporting that the cause of these differences may be a result of several bistable states created by the flow physics in the gaps between each solid rocket booster (SRB) and the rocket centerbody.

Previous computational and experimental studies have been preformed to understand the underlying flow physics governing the gap flow between two cylinders, but there is no current agreement on the mechanism that generates the bistable state [2]. Arguments have been made in favor of biased flow as a result of the Coandă effect [3], near-wake interactions [4], and losses of stability in the near wake [5]. Other potential explanations include shear layer instability, gap squeezing effects, and Kelvin-Helmholtz instabilities [2]. This type of flow has also been noted as being sensitive to Reynolds number effects and the distance between cylinders [6, 7].

Based on the data collected in the wind tunnel, this paper posits that the bistable flow state observed during testing may have been introduced by the Coandă effect. Unlike previous work focusing on two identical cylinders, this paper covers a fully instrumented rocket consisting of three integrated cylindrical bodies with variable diameter. Few studies have examined three cylinders in parallel, although three cylinders in tandem have been examined [8]. In addition, the wind tunnel test of the SLS was also conducted at a Reynolds number per core diameter range of Re_D = 4.3 x 10^5 and 6.3 x 10^5, a range of values that is one to three orders of magnitude higher than previous studies [2]. Previous CFD studies preformed by the SLS team attribute this behavior to the Coandă effect [9, 10], although this is the first time bistable flow states have been analyzed on the SLS experimentally. An analysis of time-averaged force and moment coefficient data, time-dependent force and moment coefficient data, and smoke flow images will be provided to support this hypothesis. Sample aerodynamic data will be presented, but data plots will not show absolute values of aerodynamic coefficients as the SLS program data are under International Traffic in Arms Regulations (ITAR) and Controlled Unclassified Information (CUI) restrictions.

II. Experimental Design

This work is based on a wind tunnel test that was conducted at the NASA Langley 14- by 22-Foot Subsonic Tunnel in 2021. The main purpose of the test was to collect data to generate the aerodynamic database for the Liftoff and Transition (LOT) phase of launch [11, 12]. The other main objective was to acquire data to generate the ground wind loads aerodynamic database. To accomplish this, both the 1.75%-scale SLS Block 1B Crew and SLS Block 1B Cargo test articles were tested alongside a 1.75%-scale model of the Mobile Launcher 2 (ML-2). The presence of the ML-2 in the tunnel allowed for greater accuracy quantifying the ground wind loads measured by the rocket as a result of launch tower interactions. This paper will focus on the liftoff configuration, with the test article standing upright at a total angle of attack, α, of 90°.

A. Facility Overview

The NASA Langley 14- by 22-Foot Subsonic Tunnel (Fig. 2) is a closed-circuit, single-return, atmospheric wind tunnel that can operate in a variety of test section configurations – closed, slotted, partially open, and open [13]. The closed test section is approximately 14 feet high, 22 feet wide, and 50 feet long, and has a maximum speed of about 338 ft/sec. The current test was conducted with the test section in the closed configuration, with most runs conducted at a dynamic pressure, q_∞, of 50 psf. An aerial view of the wind tunnel is shown in Fig. 3.

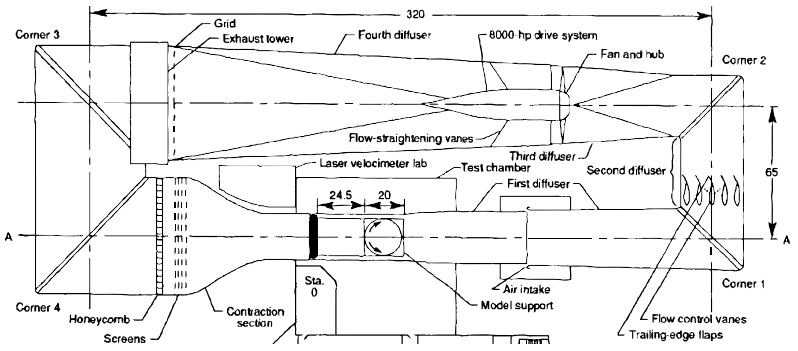

Fig. 2 Plan view of the NASA Langley 14- by 22-Foot Subsonic Tunnel [13]. Dimensions are in feet.

Fig. 3 Aerial view of the NASA Langley 14- by 22-Foot Subsonic Tunnel [14].

B. Data Acquisition

The facility's static data acquisition system (SDAS) was used to collect data throughout this wind tunnel test. After digital and analog data have passed through the appropriate signal conditioning in the model interface (MIF) cabinets and plugboard cabinets in the control room, data are processed and converted into engineering units using a Neff controller and data acquisition unit (DAU), with a user-specified sampling rate and acquisition time [15]. The acquired time-dependent data are then averaged over the eight second acquisition period before being delivered to the customer as a single data point. While it is common for the customer to only ask for the final time-averaged data during a test, the facility also keeps a record of the time-dependent data. The sampling rate was set at 50 Hz, and all analog channels had a 1 Hz low pass filter applied to reduce noise. A diagram of the data acquisition process is displayed in Fig. 4.

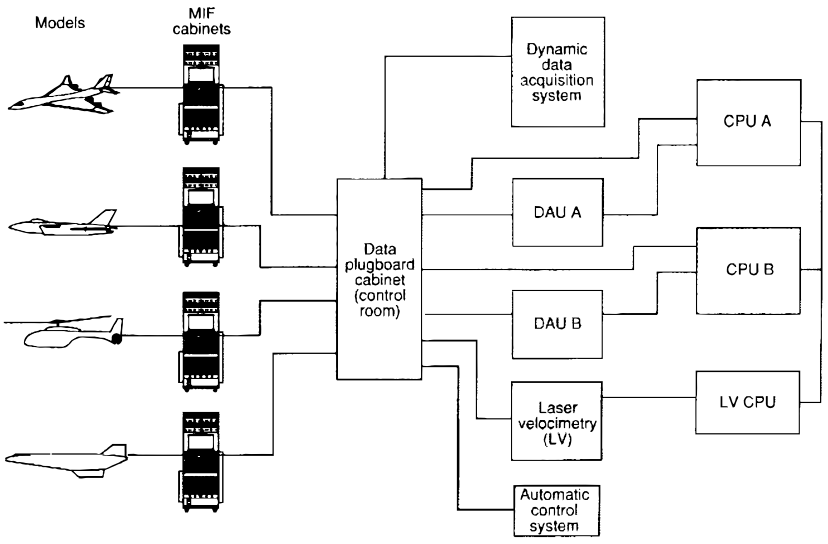

Fig. 4 Data system overview of the NASA Langley 14- by 22-Foot Subsonic Wind Tunnel [15].

C. Model Description

The wind tunnel model was a 1.75%-scale model of the full-scale SLS Block 1B Cargo and Block 1B Crew configurations. Both geometries share a common core section with an interchangeable upper stage to allow for each configuration to be tested without removing the entire model from the balances and mounting system. The liftoff phase of testing utilized the Ares post adapter installed vertically in the test section [16], with the launch tower and mobile launch platform (MLP) secured to the tunnel floor turntable. Images of the SLS Block 1B Crew and Block 1B Cargo in liftoff configuration are shown in Figures 5a and 5b, respectively.

In the liftoff phase of testing, a variable liftoff ratio was commanded in the tunnel to simulate different rocket heights in relation to the ML-2 throughout the liftoff phase. A diagram of several different h/L values is shown in Fig. 6. The parameter used to define liftoff ratio, h/L, was quantified as the ratio of the height of the SLS Block 1 configuration above the MLP to the height of the ML-2. As such, differences in the model height between the reference and actual configurations meant that the range of h/L values tested in the current test varied between h/L = -0.003 and h/L = 0.876.

The coordinate system used during the liftoff phase of testing is shown in Fig. 7. The turntable could be rotated to any desired wind azimuth angle between 0° and 360°, with the exception of a mechanical deadband between wind azimuth angles of ψ_{azm} = 75° to 105°. The deadband was placed in this location because previous tests demonstrated model behavior was relatively symmetric in this region when compared to the ψ_{azm} = 250° through 290° region [11, 12].

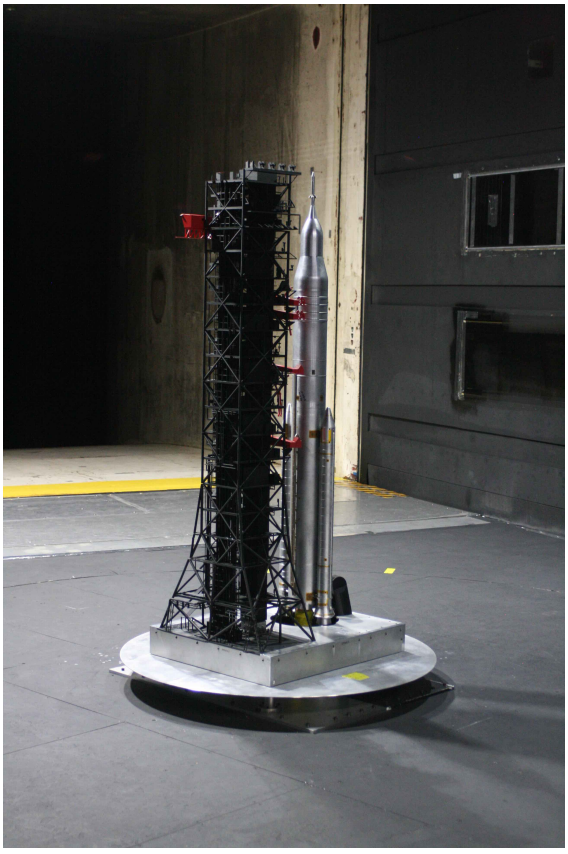

(a) SLS Block 1B Crew with ML-2 installed.

(b) SLS Block 1B Cargo with ML-2 installed.

Fig. 5 SLS liftoff configurations.

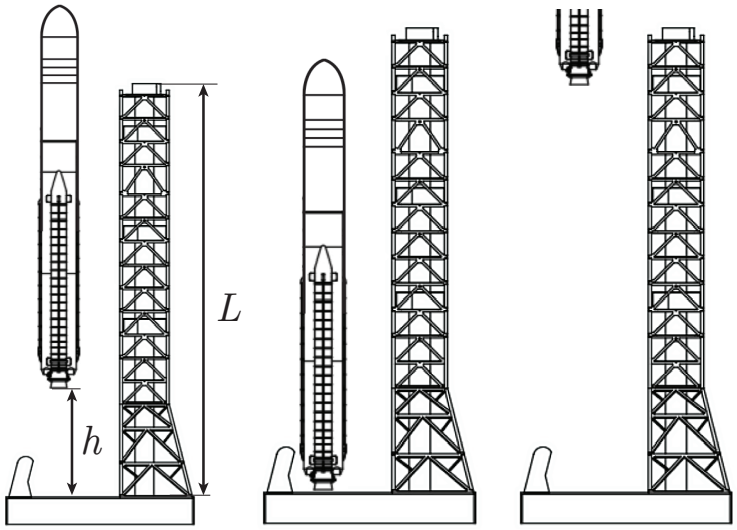

(a) h/L definition (b) h/L = -0.003 (c) h/L = 0.876

Fig. 6 Launch vehicle elevation with respect to the ML-2 height (h/L) and limiting cases in the present test campaign [12].

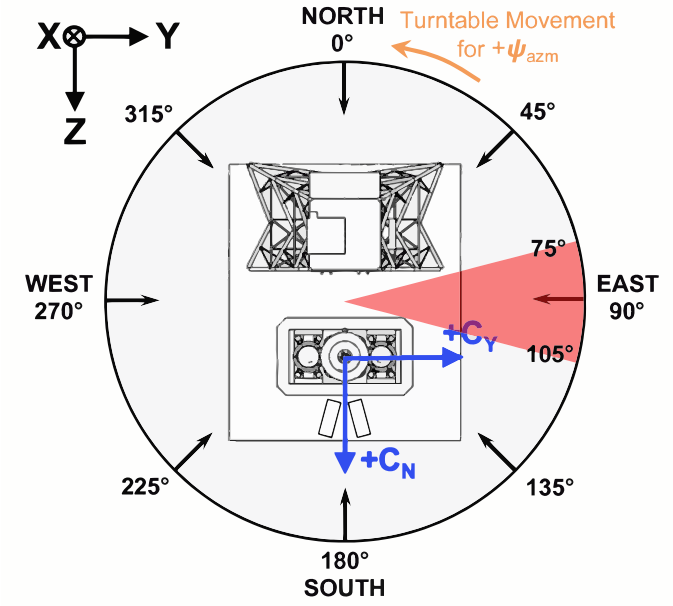

Fig. 7 Coordinate system used during liftoff phase of testing (mechanical deadband highlighted in red) [12].

D. Instrumentation

Figure 8 shows the main components of the 1.75%-scale model assembly. The VST-15 balance was used to measure force and moment data for the entire full stack model. This balance was installed to the 1.5D-to-2.5D sting and to the model block, and the common core stage was installed to the model block. The upper stage was attached to the common core stage. Force and moment data were also acquired for each SRB through the use of two ATI Industrial Automation (ATI-IA) Mini45 load cells per booster as mounted to the vehicle centerbody. These measurements were independent of the full stack force and moment measurements provided by the VST-15 balance.

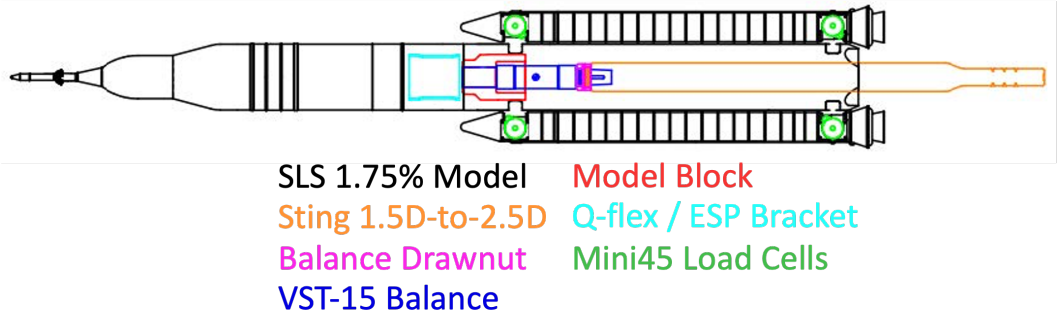

Fig. 8 Main components of the 1.75%-scale SLS vehicle model assembly.

Static pressure data were acquired throughout the test at a variety of different longitudinal stations and azimuthal locations. For the Block 1B Crew configuration, a total of 34 core pressures, 28 upper stage pressures, and 6 base pressures were collected. For the Block 1B Cargo configuration, a total of 34 core pressures, 61 upper stage pressures, and 6 base pressures were collected. The azimuthal locations of the pressure ports are defined in Fig. 9.

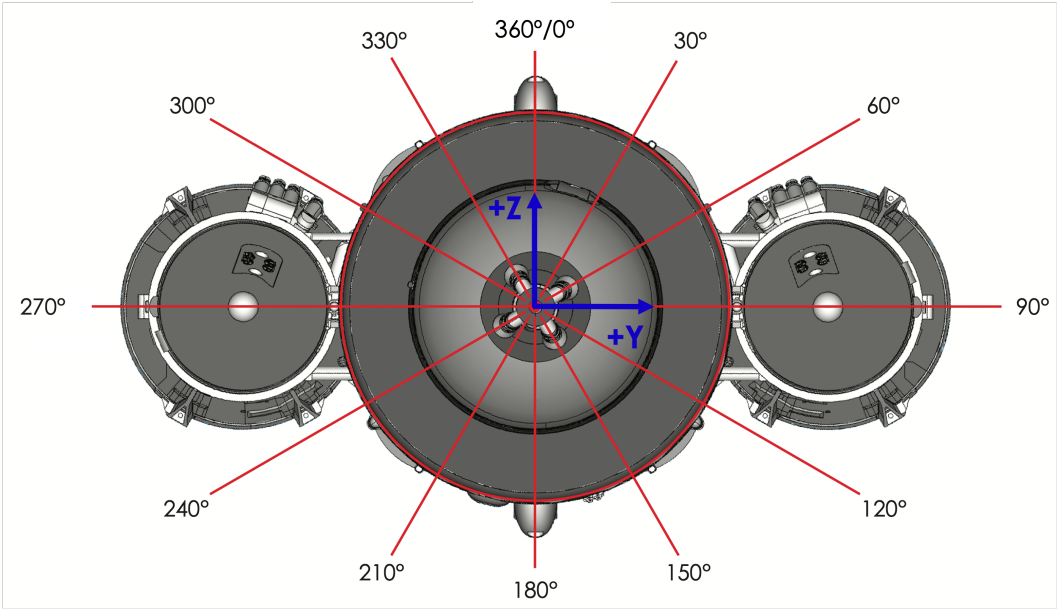

Fig. 9 Pressure port azimuthal locations.

E. Flow Visualization

Smoke flow visualization was performed on the model, both with ML-2 present and ML-2 removed. The commercial smoke flow generator system utilized heated proplyene glycol for the smoke stream and compressed air to produce an aerosol that closely tracks the airflow. One engineer was placed in the test section holding the smoke wand. This engineer was accompanied by another engineer inside of the tunnel to take photos of the smoke flow interacting with the test article. A third engineer was positioned with a camera above the test section to take overhead views throughout the smoke flow runs. In addition to the two cameras, the facility provided video camera footage from four different angles looking into the test section to view the smoke behavior in real time. The application of smoke flow aided in the understanding of the potential Coandă effect behavior witnessed throughout the test. Before performing smoke flow, the test section floor was painted black to provide better contrast between the smoke and the floor. Smoke flow runs were performed at q_∞ = 3.5 psf. An image of the model with smoke flow applied is shown in Fig. 10.

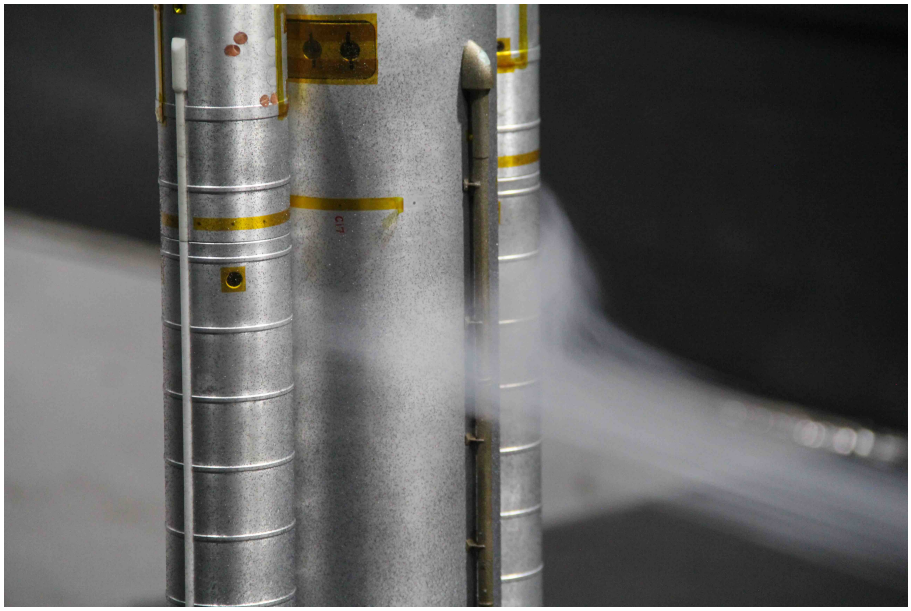

Fig. 10 SLS Block 1B Crew model with smoke flow applied.

Toward the conclusion of smoke flow testing, tufts were applied to the model to aid with visualizing the behavior of the flow directly downstream of the gap between the SRBs and the rocket centerbody. A view of the model with tufts applied is shown in Fig. 11.

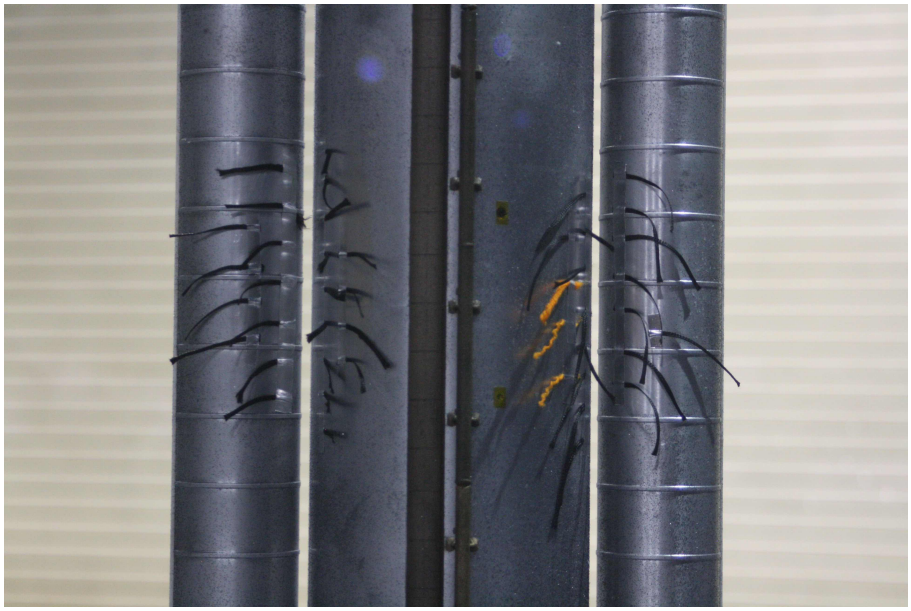

Fig. 11 SLS Block 1B Crew model with tufts applied.

III. Discussion of Results

A. Time-Averaged Data

Force and moment repeatability discrepancies were first observed on the full-stack force and moment coefficients at the beginning of the liftoff phase of testing. This behavior was not expected by the test team, as previous tests suggested repeatability was strong [12]. Furthermore, the transition runs conducted up to that point showed good repeatability, leading the team to hypothesize that potential flow phenomena may be occurring as a result of the model's orientation in the liftoff position, where it assumes a fixed total angle of attack, α, of 90°.

Time-averaged forebody force and moment coefficients from a pair of azimuth wind angle sweeps are presented in Fig. 12. The data from this case are derived from a pair of repeat runs (Run 303 and Run 321) with the SLS Block 1B Crew configuration. The ML-2 was installed, and the liftoff ratio h/L was set at -0.003, which corresponds to the prelaunch vehicle position relative to the tower. Both runs were conducted at a dynamic pressure q_∞ = 50 psf. Note the highlighted discrepancy region bounded by the blue lines between ψ_{azm} = 150° and ψ_{azm} = 220°.

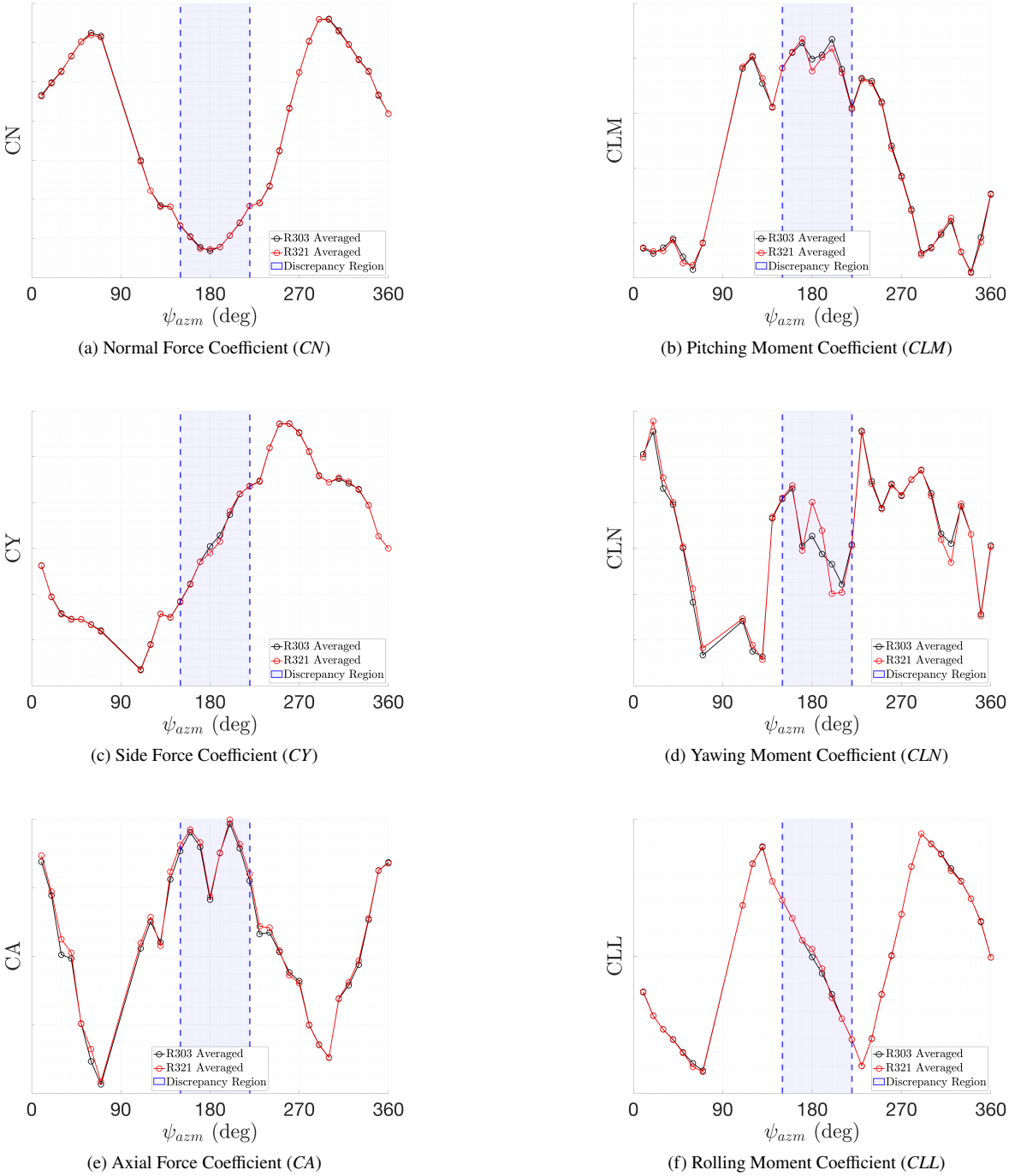

(a) Normal Force Coefficient (*CN*)

(b) Pitching Moment Coefficient (*CLM*)

(c) Side Force Coefficient (*CY*)

(d) Yawing Moment Coefficient (*CLN*)

(e) Axial Force Coefficient (*CA*)

(f) Rolling Moment Coefficient (*CLL*)

Fig. 12 Time-averaged full-stack force and moment coefficient data, SLS Block 1B Crew, ML-2 installed, h/L = -0.003, q_∞ = 50 psf.

The variation of side force coefficient, *CY*, with wind azimuth angle is shown in Fig. 12c. Agreement is strong with the exception of the center of the discrepancy region, at wind angles between ψ_{azm} = 180° through ψ_{azm} = 200°. While this appears to be a small difference graphically, the average percent difference in this region increases from around ±1% to well over 10% here. This magnitude of difference is significant and must be taken into account when constructing an aerodynamic database from this set of data. Significant differences are also present in the yawing moment coefficient, *CLN*, (Fig. 12d), the pitching moment coefficient, *CLM*, (Fig. 12b), and the rolling moment coefficient, *CLL*, (Fig. 12f).

Several measurement influences were evaluated to determine if instrument-related effects were causing the observed behavior. This is unlikely, however, as the differences only appeared in a localized region of wind angle azimuths and the temperatures varied by no more than 10°F between corresponding test points in the run comparison shown above. Another potential influence was that differences were caused by hysteresis, but this is also unlikely, as the example above showed two different sweeps that were both performed in the same direction. Finally, it was proposed that differences were caused by an asymmetric vortex coming off the rocket centerbody and acting on the central beam of the ML-2, but this was discredited after runs with the ML-2 removed yielded the same behavior. Removal of the ML-2 also created discrepancy regions between ψ_{azm} = 330° and ψ_{azm} = 30°, suggesting that the presence of the tower improved repeatability, and did not hinder it.

This investigative process led to the current working theory and the basis of this paper, that the regions of poor repeatability are a result of the Coandă effect acting on the narrow gaps between the three cylindrical bodies that make up the test article, i.e., two SRBs and the rocket centerbody. If there was only one cylindrical body, there would be no gap to form a wall jet and the flow would remain attached to both sides of the cylinder as described by the Coandă effect [17]. In this test, the instability of the flow in the gaps between the SRBs and the centerbody could cause the flow to bias toward one side or the other in a bistable state on each booster, creating an asymmetric net pressure on the rocket acting in the direction normal to the wind. The wind contacts all three bodies head on at ψ_{azm} values of 180° and 0°, so this is where the effect is likely to be the most powerful. The behavior of the time-averaged data in Fig. 12 supports that the Coandă effect may be the cause of the differences, as the discrepancies only occur when the flow contacts all three bodies head on and the different values could represent the forces and moments being recorded when the flow is attached to the cylindrical bodies in two different states. Furthermore, while differences are observable at ψ_{azm} = 180°, they are not seen at ψ_{azm} = 0° when the ML-2 is installed, which shields the rocket from the flow to a certain degree and prevents any bistable behavior due to the Coandă effect from happening in the example above. When the ML-2 is not installed, the bistable behavior manifests at both the ψ_{azm} = 180° and ψ_{azm} = 0° range.

The variation of normal force coefficient, *CN*, with wind azimuth angle is shown in Fig. 12a. Unlike many of the other coefficients, normal force repeats quite strongly in the discrepancy region. Regarding normal force, this behavior may support the presence of the Coandă effect acting between the SRB gaps. Within the discrepancy region, the wind is coming from the South (ψ_{azm} values at or near 180°) and is acting almost purely in the direction of -*CN*. While *CN* remains relatively constant, *CLM* does not. This is likely due to changes in the distribution of where the forces are acting on the model, and if the Coandă effect or another bistable flow phenomena is present, these changes are likely occurring in and around where the SRBs and centerbody interface. To further investigate this claim, an in-depth discussion of the SRB effects on repeatability is provided in a later section.

The variation of axial force coefficient, *CA*, with wind azimuth angle is shown in Fig. 12e. Similar to normal force, axial force repeats well in the discrepancy region. However, it is important to note that data from this component were difficult to quantify accurately during the test. Axial force values were not a high priority during this test campaign, and in the context of the presence of any bistable flow state, *CA* is an out-of-plane measurement.

B. Time-Dependent Data

If a bistable state due to the Coandă effect or other gap flow physics was present, then it may be possible to capture the periodic switching of the flow states over the course of an eight second data point. The data plotted in Fig. 13 are the time-dependent forebody force and moment coefficients that correspond to the ψ_{azm} = 200° data points in Fig. 12 for Runs 303 and 321. The dashed lines in Fig. 13 represent the time-averaged values plotted in Fig. 12.

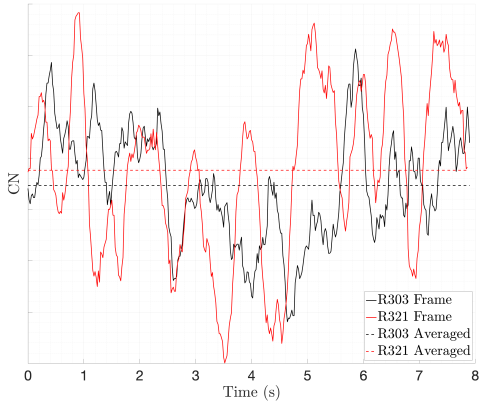

(a) *CN*

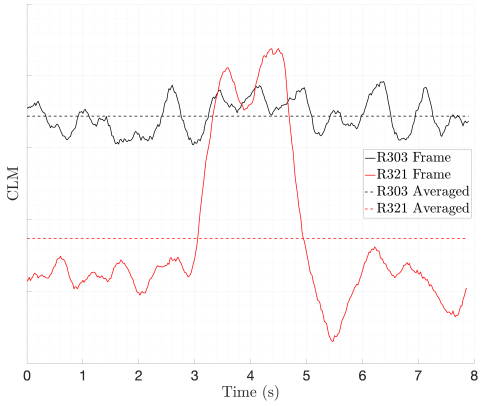

(b) *CLM*

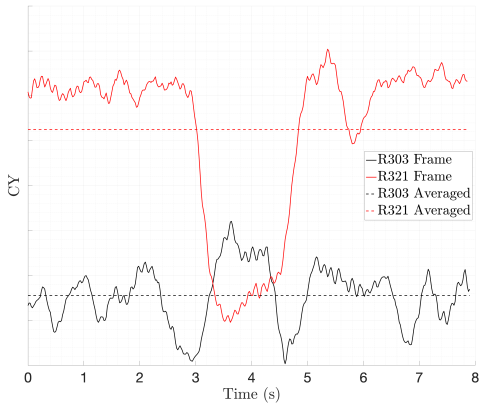

(c) *CY*

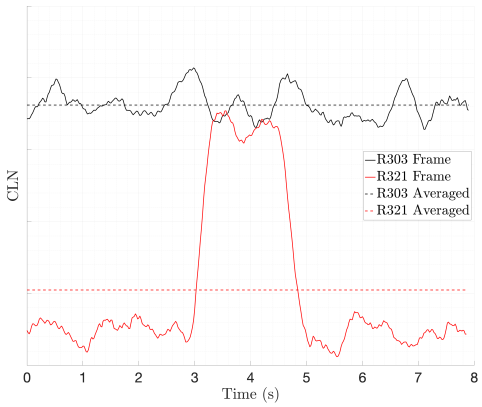

(d) *CLN*

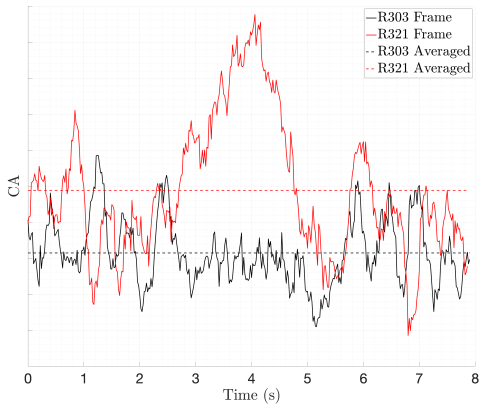

(e) *CA*

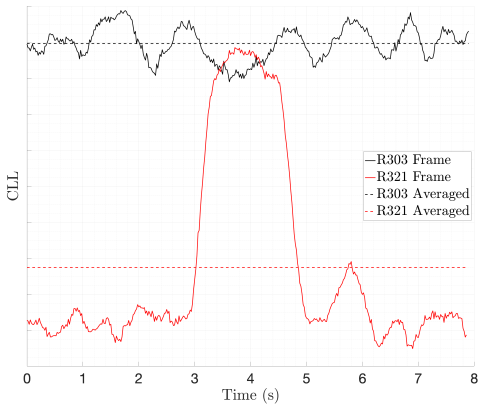

(f) *CLL*

Fig. 13 Time-dependent full-stack force and moment coefficients, SLS Block 1B Crew, ML-2 installed, ψ_{azm} = 200°, h/L = -0.003, q_∞ = 50 psf.

The time-dependent force and moment coefficients at this condition provide strong evidence for the presence of a bistable flow state that could potentially be created as a result of the Coandă effect. Between time $t = 0$ and $t = 3$ seconds, each run appear to be oscillating around different mean values, or two different states. However, between $t = 3$ and $t =$

5 seconds there is a noticeable change in the behavior of the Run 321 data point. All four coefficients that had repeated poorly in this region, namely *CLN* (Fig. 13d), *CY* (Fig. 13c), *CLM* (Fig. 13b), and *CLL* (Fig. 13f), dramatically change in value and begin to oscillate around the same mean values as the repeat Run 303 data point. After briefly 'snapping' to the other bistable state, the Run 321 data point then returns to its original state for the remainder of the eight second test point. It is hypothesized that the two stable states may be a result of the Coandă effect, and the behavior of the time-dependent data supports this. It is important to note that the switching between states appears to be random when in this unsteady region, which could explain why this behavior was not observed in previous tests. Few repeat runs of the liftoff configuration were conducted in the past, and the ones that were performed may have been fortunate enough to capture data in the same flow state each time. A representation of potential flow states is shown in Fig. 14. When the freestream approaches all three cylindrical bodies of the rocket most directly, at or close to $\psi_{azm} = 180°$, the flow could settle into and then change between any one of these four states.

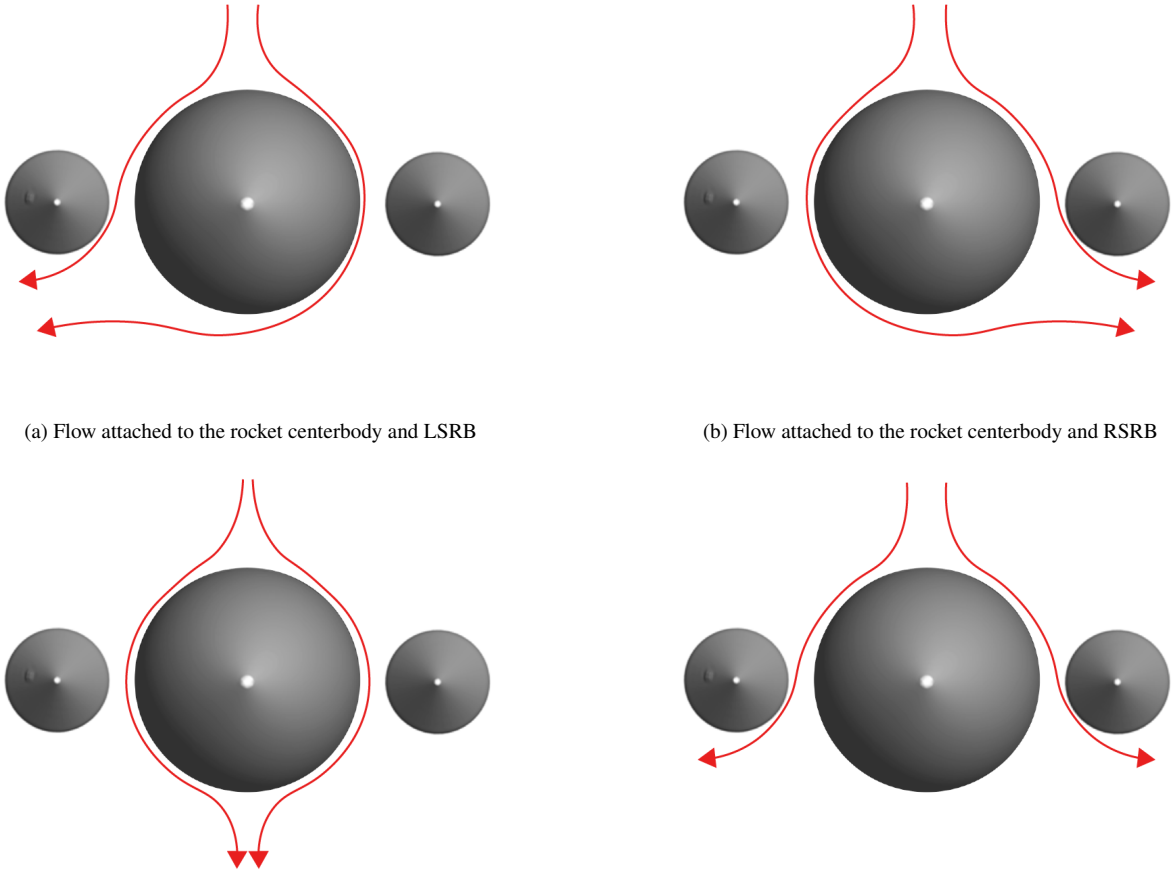

(a) Flow attached to the rocket centerbody and LSRB

(b) Flow attached to the rocket centerbody and RSRB

(c) Flow attached to the rocket centerbody alone

(d) Flow attached to the RSRB and LSRB

Fig. 14 Streamline traces of potential flow states, $\psi_{azm} = 180°$ [18].

While the swapping between states is easily observable between $t = 3$ and $t = 5$ seconds for the four aforementioned coefficients, this is not the case for the normal force coefficient *CN* (Fig. 13a). This is consistent with what was observed in the time-averaged behavior of this coefficient. As such, the time-averaged normal force values are very similar and the time-dependent data appear to oscillate around similar values.

In order to determine whether or not the presence of any bistable flow states were localized to within the ψ_{azm} discrepancy region between 150° and 220°, time-dependent cases were analyzed at wind azimuth angles that occur outside of the discrepancy region, where repeatability was stronger. A representative case at $\psi_{azm} = 250°$ is shown in

Fig. 15. The same pair of repeat runs from the previous plots, Run 303 and Run 321, were used for this comparison.

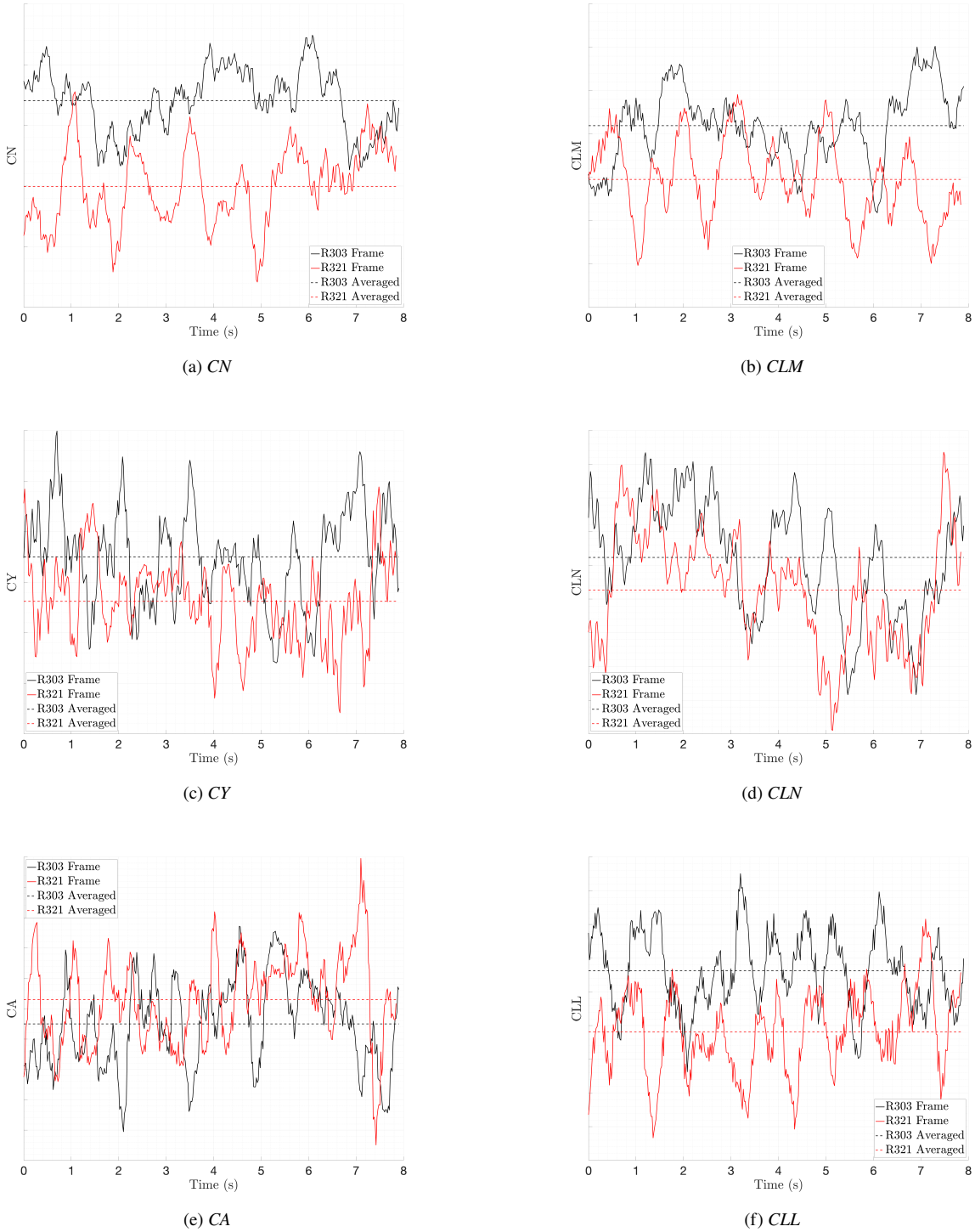

(a) *CN* (b) *CLM*

(c) *CY* (d) *CLN*

(e) *CA* (f) *CLL*

Fig. 15 Time-dependent full-stack force and moment coefficients, SLS Block 1B Crew, ML-2 installed, ψ_{azm} = 250°, h/L = -0.003, q_∞ = 50 psf.

This behavior supports the theory that the variable flow states are localized to within the discrepancy region, as there is no observable evidence of any switching of states in the ψ_{azm} = 250° case. If the Coandă effect was observed during

data collection, it would most likely manifest in *CLN* (Fig. 15d), *CY* (Fig. 15c), *CLM* (Fig. 15b), or *CLL* (Fig. 15f). However, while there are small differences in the time-averaged coefficient values between runs, the time-dependent data oscillate firmly around their averages and do not take any large departures throughout the 8 second data collection window. As such, any differences in the force and moment coefficients are likely not a result of any sort of flow state switching at this condition. This is in contrast to Fig. 13, where a large departure from the time-averaged values is observable between t = 3 and t = 5 seconds. Note that while only one representative case outside of the discrepancy region is presented as evidence, the state-switching behavior was not observed in any of the other repeat run pairs and wind azimuth angles outside of the aforementioned discrepancy region.

C. SRB Data

After observing state-switching behavior in the time-dependent forebody force and moment data, the time-dependent integrated balance data for each SRB was analyzed. This allowed for the contribution of each individual SRB to the observed lack of repeatability to be determined.

The time-dependent LSRB force and moment coefficients that correspond to the ψ_{azm} = 200° data points for Runs 303 and 321 are plotted in Fig. 16. The dashed lines in Fig. 16 represent the time-averaged force and moment coefficients for the LSRB for each of the aforementioned runs. The time-dependent RSRB data for the same run pair are shown in Fig. 17. The dashed lines in Fig. 17 represent the time-averaged force and moment coefficients for the RSRB for each of the aforementioned runs. Note that corresponding coefficients for both the LSRB and RSRB data are plotted on ordinate axes of the same relative magnitude to allow for differences between each SRB to be visualized more clearly.

The variation of side force coefficient over the eight second sampling period is shown for the LSRB (*BLCY*) in Fig. 16c and for the RSRB (*BRCY*) in Fig. 17c. Each booster exhibits different behavior at this condition. While *BLCY* appears to oscillate around different average values throughout the entire sampling period, *BRCY* clearly swaps to a different state between t = 3 and t = 5 seconds, in a manner akin to what was observed on the forebody *CY* data (Fig. 13c). This implies that while each SRB may have settled on a different flow state (as evidenced by their differing time-averaged values), they don't necessarily exhibit state-switching at the same time. In this case, the RSRB appears to have switched states fully while the LSRB has not. Similar behavior can be observed in yawing moment coefficients *BLCLN* and *BRCLN* in Figs. 16d and 17d, as well as in rolling moment coefficients *BLCLL* and *BRCLL* in Figs. 16f and 17f. For each of these coefficients, the flow acting on the RSRB dramatically switches states, while the flow acting on the LSRB does not. Both axial force coefficients *BLCA* (Fig. 16e) and *BRCA* (Fig. 17e) do not appear to be particularly sensitive to any switching of flow states, and oscillate around slightly different values as expected.

While the four aforementioned coefficients appear to provide evidence for a bistable state on the RSRB and not the LSRB, the remaining two coefficients show that this may not entirely be the case. The variation in pitching moment coefficient over the eight second sampling period is shown for the LSRB (*BLCLM*) in Fig. 16b and for the RSRB (*BRCLM*) in Fig. 17b. Unlike in previous coefficients where the LSRB does not appear to be switching states, there is a large spike in *BLCLM* between t = 3 and t = 5 seconds, while there is almost no discernible spike in *BRCLM*. Furthermore, contrasting behavior can be observed in the LSRB normal force coefficient (*BLCN*) in Fig. 16a and in the RSRB normal force coefficient (*BRCN*) in Fig. 17a. Both *BLCN* and *BRCN* exhibit a spike in value over the same t = 3 and t = 5 second period, but the *BRCN* spike is of a larger magnitude. One potential explanation for this inconsistent behavior is that, for the LSRB, the trends shown by *BLCN* and *BLCLM* are an example of partial state-switching. If the flow acting across the entire SRB changes states at the same time, a large jump in normal force but little to no change in pitching moment would be expected, due to the even distribution of loads on the booster. This is similar to what was observed in the RSRB data. However, if only part of the SRB changes states, then this is likely to show as a change both in normal force and pitching moment due to a now unevenly balanced distribution of loads across the booster (assuming the section that changed states wasn't centered on the balance moment center). Using this argument, it is hypothesized that the gap flow between the RSRB and core experienced a full swapping of states, while the gap flow between the LSRB and core may only have partially changed states. This may be due to the wind angle ψ_{azm} = 200°, meaning that the wind is approaching at an angle that isn't completely head on at 180° as it goes through the SRB gaps. This may cause only one SRB to fully switch and not the other.

In summary, both the LSRB and RSRB data show compelling results that support the presence of a bistable flow state at each SRB that could be explained by the Coandă effect. After reviewing the time-dependent data, state-switching is definitely present in the RSRB data and may be occurring partially in the LSRB data. Either way, though, the flow physics interacting between the SRBs and the rocket centerbody are contributing to the observed lack of repeatability.

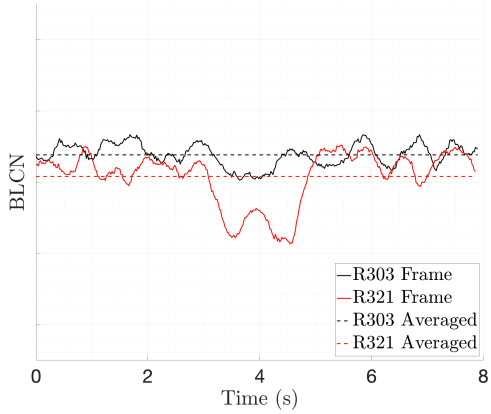

(a) LSRB Normal Force Coefficient (*BLCN*)

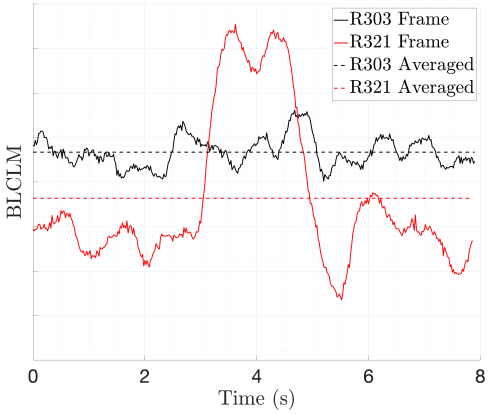

(b) LSRB Pitching Moment Coefficient (*BLCLM*)

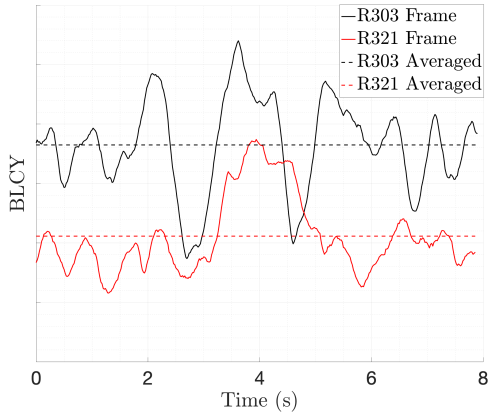

(c) LSRB Side Force Coefficient (*BLCY*)

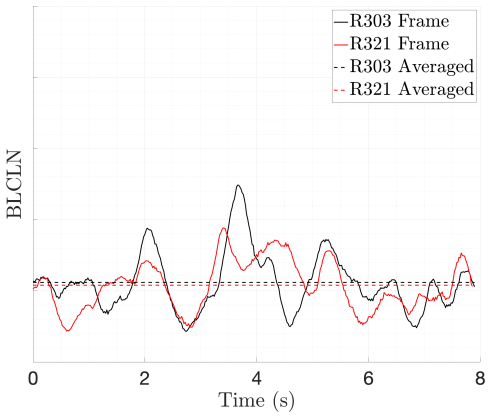

(d) LSRB Yawing Moment Coefficient (*BLCLN*)

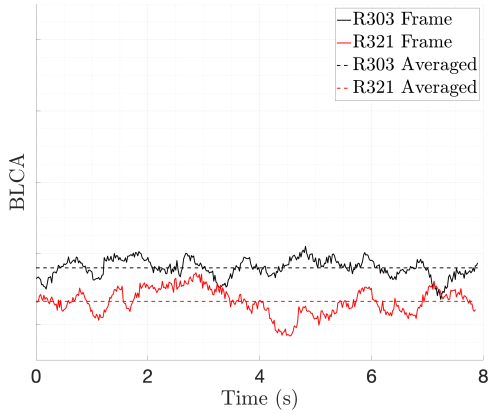

(e) LSRB Axial Force Coefficient (*BLCA*)

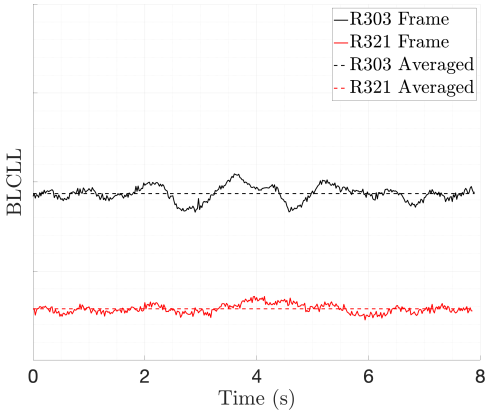

(f) LSRB Rolling Moment Coefficient (*BLCLL*)

Fig. 16 Time-dependent LSRB force and moment coefficients, SLS Block 1B Crew, ML-2 installed, ψ_{azm} = 200°, h/L = -0.003, q_∞ = 50 psf.

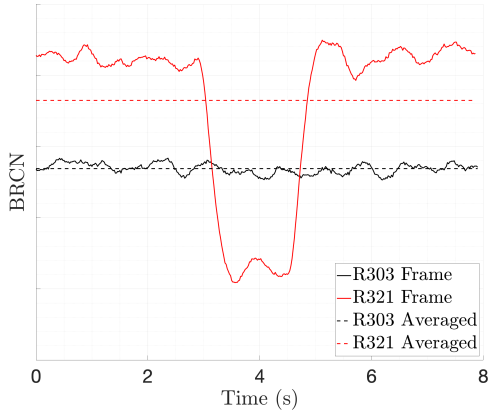

(a) RSRB Normal Force Coefficient (*BRCN*)

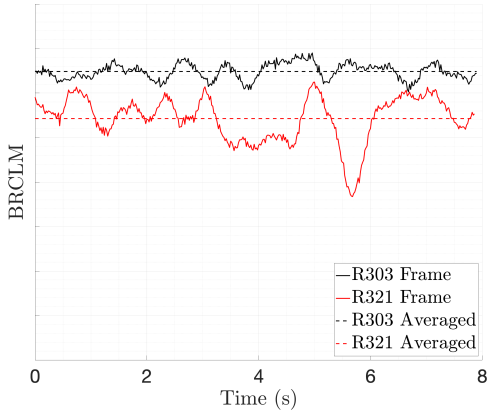

(b) RSRB Pitching Moment Coefficient (*BRCLM*)

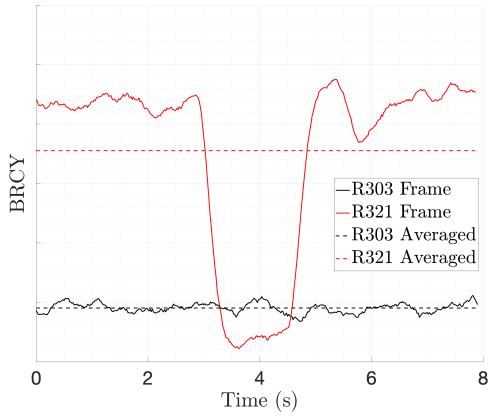

(c) RSRB Side Force Coefficient (*BRCY*)

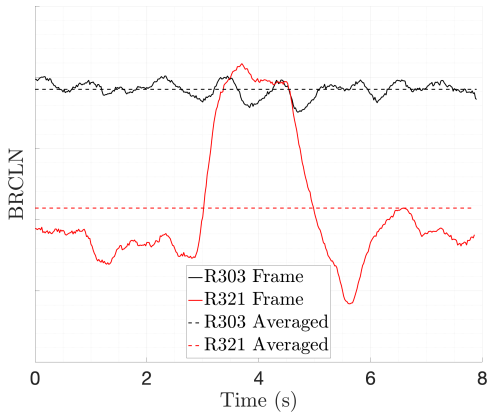

(d) RSRB Yawing Moment Coefficient (*BRCLN*)

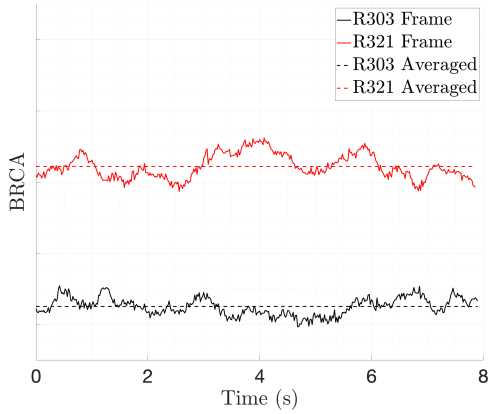

(e) RSRB Axial Force Coefficient (*BRCA*)

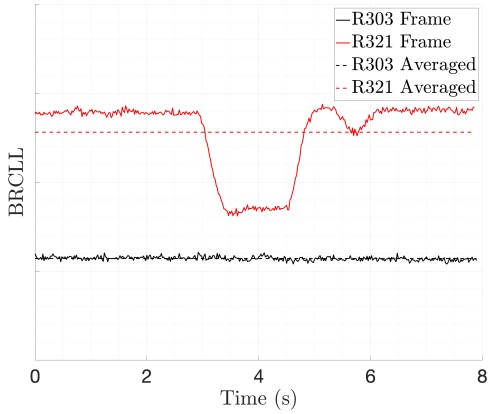

(f) RSRB Rolling Moment Coefficient (*BRCLL*)

Fig. 17 Time-dependent RSRB force and moment coefficients, SLS Block 1B Crew, ML-2 installed, ψ_{azm} = 200°, h/L = -0.003, q_∞ = 50 psf.

D. Flow Visualization Results

Flow visualization runs provided further evidence supporting the presence of multiple flow states occurring as a result of the Coandă effect. Three representative screenshots from a smoke flow visualization run with tufts applied are shown in Fig. 18. In order to best recreate the flow conditions where the force and moment discrepancies were noticed, the wind azimuth angle was set to ψ_{azm} = 180° and the liftoff ratio, h/L, was set at -0.003. The dynamic pressure, q_∞, was set to 3.5 psf instead of the typical 50 psf to provide a safe representative flow environment for the engineers located within the test section during data collection.

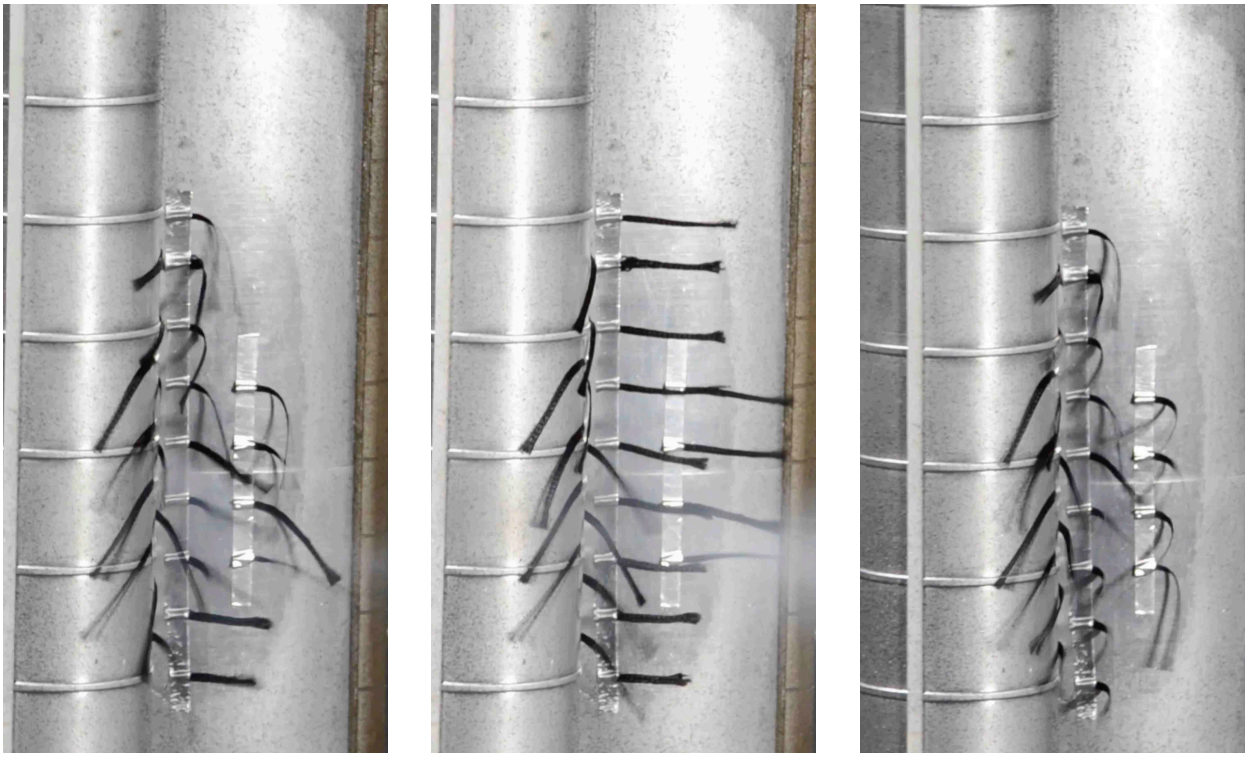

(a) Period 1 (4 second duration) (b) Period 2 (8 second duration) (c) Period 3 (8 second duration)

Fig. 18 Smoke flow visualization with tufts applied to SLS Block 1B Crew centerbody and SRBs, ψ_{azm} = 180°, h/L = -0.003, q_∞ = 3.5 psf.

A snapshot acquired during Period 1, which spans the first four seconds of data collection, is shown in Fig. 18a. During this time period, the tufts on the LSRB are loosely attached to the booster surface. The tufts on the rocket centerbody appear to be drawn toward the SRB gap, with the exception of two tufts at the aft end of the centerbody. However, this behavior changes in Period 2 (Fig. 18b), which consists of an eight second time window following Period 1. While the tufts on the LSRB remained unchanged, the tufts on the rocket centerbody experienced a noted difference in behavior, with all of them going from being loosely pulled toward the SRB gap to tightly attached to the surface of the rocket centerbody. This is a visual representation of the Coandă effect at work, and shows how the flow is able to randomly switch between different states by attaching to different surfaces on the test article. After remaining attached to the centerbody for an eight second period, the flow returns to the original state in Period 3 (Fig. 18c), which covers an eight second time window following Period 2. Note that the behavior of the tufts was observed both with and without the use of the smoke flow wand, so it is unlikely that results were influenced by the introduction of the smoke into the freestream.

In the context of data acquisition during a wind tunnel run, the results from flow visualization show that for a representative run at q_∞ = 50 psf with no tufts on the model, it is impossible to know what state the flow will be in during the acquisition of an eight second data point at wind azimuth angles where the Coandă effect was observed. This state-dependent behavior provides a potential explanation as to why a lack of repeatability was observed for some runs during the test, but not for all of them. It is recommended that any aerodynamic database constructed with this

data should account for this behavior when quantifying uncertainties around the regions where the Coandă effect is present.

IV. Conclusion

This work introduced and investigated the hypothesized presence of the Coandă effect as a potential explanation for the discrepancies between repeat runs observed during the 2021 14-Foot by 22-Foot Subsonic Tunnel test of the Space Launch System in the liftoff configuration. Supporting evidence was provided through an examination of time-averaged force and moment coefficient data, time-dependent force and moment coefficient data, and images collected during flow visualization runs.

The time-dependent force and moment coefficient data supported the presence of a bistable state at wind azimuth angles where the freestream contacted the gaps between the rocket centerbody and SRBs head on. These angles varied depending on configuration, but repeatability issues were typically observed between ψ_{azm} = 150° and ψ_{azm} = 220° for runs with the ML-2 installed, and between ψ_{azm} = 330° and ψ_{azm} = 30° in addition to the former range when the ML-2 was removed and no longer able to shield the test article from the flow. At these wind azimuth angles of interest, the flow attached to either the respective SRB or the centerbody at each gap, meaning that there were two bistable states present, or four states in total. As such, the time-averaged force and moment coefficient data had the potential to repeat poorly depending on which state the rocket was experiencing during the eight second data collection window.

Video evidence from tuft and smoke flow visualization runs also confirmed the presence of multiple flow states. Tufts were attached to the test article slightly downstream of the SRB and centerbody gaps, and wind-on runs visually demonstrated that the tufts randomly switched between two different states near each booster gap.

The potential to collect force and moment data from a total of four different flow states while at the same condition could create issues when constructing an aerodynamic database. All of the states are equally valid, but each one has different force and moment values associated with it. It would be impractical to attempt to collect data from each individual state due to the random behavior of the flow, so the recommended solution is to increase the quantified uncertainty values for all database coefficients while in the discrepancy range. This recommendation was adopted in the final released version of the SLS Block 1B Crew static ground wind loads database, and this source of uncertainty would not have been included were it not for the efforts to explore the phenomena that was observed in the wind tunnel and outlined in this paper. To better understand this complex flow behavior, it would be pertinent to perform more computational and experimental efforts at similar test conditions in the future.

Acknowledgments

The authors would like to thank the model design engineers, the research team, and the force measurement engineers for their constant support throughout the testing process. The authors would also like to thank Brandon Caudill, Sam Zauber, and the other members of the 14-Foot by 22-Foot Subsonic Tunnel team that helped support the experimental data collection process. Finally, the authors would like to thank the SLS program and the SLS Aerodynamics Task Team for their support of this work.

References

[1] "Space Launch System," Available at `https://www.nasa.gov/exploration/systems/sls/index.html`, Accessed: 10/15/2021.

[2] Wu, G., Lin, W., Du, X., Shi, C., and Zhu, J., "On the flip-flopping phenomenon of two side-by-side circular cylinders at a high subcritical Reynolds number of 1.4 x 10^5," *Phys. Fluids*, Vol. 32, No. 9, 2020, p. 094112.

[3] Ishigai, S., Nishikawa, E., Nishimura, K., and Cho, K., "Experimental study on structure of gas flow in tube banks with tube axes normal to flow (Part 1, karman vortex flow from two tubes at various spacings," *Bull. JSME*, Vol. 15, No. 86, 1972, pp. 949–956.

[4] Bearman, P. W., and Wadcock, A. J., "The interaction between a pair of circular cylinders normal to a stream," *J. Fluid Mech.*, Vol. 61, No. 3, 1973, pp. 499–511.

[5] Bai, X., Zhang, W., Guo, A., and Wang, Y., "The flip-flopping wake pattern between two side-by-side circular cylinders: A global stability analysis," *Phys. Fluids*, Vol. 28, No. 4, 2016, p. 044102.

[6] Xu, S. J., Zhou, Y., and So, R. M. C., "Reynolds number effects on the flow structure behind two side-by-side cylinders," *Phys. Fluids*, Vol. 15, No. 5, 2003, pp. 1214–1219.

[7] Singha, S., Nagarajan, K. K., and Sinhamahpatra, K. P., "Numerical study of two-dimensional flow around two side-by-side circular cylinders at low Reynolds numbers," *Phys. Fluids*, Vol. 28, No. 5, 2016, p. 053603.

[8] Zdravkovich, M. M., and Pridden, D. L., "Intereference between two circular cylinders; series of unexpected discontinuities," *J. Wind Eng. Ind. Aeryodn.*, Vol. 2, No. 3, 1977, pp. 255–270.

[9] Krist, S. E., Ratnayake, N. A., and Ghaffari, F., "Kestrel Results at Liftoff Conditions for a Space Launch System Configuration in Proximity to the Launch Tower," *AIAA AVIATION Forum*, 2019.

[10] Ratnayake, N. A., Krist, S. E., Ghaffari, F., and Deere, K. A., "Computational Fluid Dynamics Methods Used in the Development of the Space Launch System Liftoff and Transition Lineloads Databases," *AIAA AVIATION Forum*, 2019.

[11] Pinier, J. T., Erickson, G. E., Paulson, J. W., Tomek, W. G., Bennett, D. W., and Blevins, J. A., "Aerodynamic Characterization and Improved Testing Methods for the Space Launch System Liftoff and Transition Environment," 2015, AIAA Paper 2015-0775.

[12] Chan, D. T., Paulson, J. W., Shea, P. R., Toro, K. G., Parker, P. A., and Commo, S. A., "Aerodynamic Characterization and Improved Testing Methods for the Space Launch System Liftoff and Transition Environment," *AIAA Aviation Forum*, 2019.

[13] Gentry, C. L., Quinto, P. F., Gatlin, G., and Applin, Z., "The Langley 14- by 22-Foot Subsonic Tunnel: Description, Flow Characteristics, and Guide for Users," 1990, NASA-TP-3008.

[14] "Aerials of Langley Research Center," Available at `https://images.nasa.gov`, Accessed: 10/15/2021.

[15] Quinto, P. F., and Orie, N. M., "Langley 14- by 22-Foot Subsonic Tunnel Test Engineer's Data Acquistion and Reduction Manual," 1994, NASA-TM-4563.

[16] Capone, F. J., Paulson, J. W., and Erickson, G. E., "Liftoff and transition aerodynamics of the Ares I (A106) launch vehicle," *Journal of Spacecraft and Rockets*, Vol. 49, 2012, pp. 564–573.

[17] Willie, R., and Fernholz, H., "Report on the first European Mechanics Colloquium, on the Coanda Effect," *Fluid Mech.*, Vol. 23, No. 4, 1965, pp. 801–819.

[18] Pomeroy, B. W., and Krist, S. E., "Validation of Kestrel IDDES Simulations for SLS Transition Analysis," *AIAA Scitech Forum*, 2022.